How to cite: Angew. Chem. Int. Ed. 2024, e202403116
doi.org/10.1002/anie.202403116

Nanocrystals Hot Paper

Single Crystal and Pentatwinned Gold Nanorods Result in Chiral Nanocrystals with Reverse Handedness

Kyle Van Gordon[+], Bing Ni[+], Robin Girod[+], Mikhail Mychinko, Francisco Bevilacqua, Sara Bals, and Luis M. Liz-Marzán**

Dedicated to Professor Alexander Eychmüller on the occasion of his retirement.

Abstract: Handedness is an essential attribute of chiral nanocrystals, having a major influence on their properties. During chemical growth, the handedness of nanocrystals is usually tuned by selecting the corresponding enantiomer of chiral molecules involved in asymmetric growth, often known as chiral inducers. We report that, even using the same chiral inducer enantiomer, the handedness of chiral gold nanocrystals can be reversed by using Au nanorod seeds with either single crystalline or pentatwinned structure. This effect holds for chiral growth induced both by amino acids and by chiral micelles. Although it was challenging to discern the morphological handedness for *L*-cystine-directed particles, even using electron tomography, both cases showed circular dichroism bands of opposite sign, with nearly mirrored chiroptical signatures for chiral micelle-directed growth, along with quasi-helical wrinkles of inverted handedness. These results expand the chiral growth toolbox with an effect that might be exploited to yield a host of interesting morphologies with tunable optical properties.

Introduction

Chirality can be transferred from organic to inorganic substances, via assembly of achiral building blocks into a chiral arrangement, or by the preparation of nanostructures with chiral morphology.[1] This has been historically accomplished by directing amino acids or peptides to systems such as $CaCO_3$,[2–3] Au,[4–7] Ag,[8] HgS,[9] or Te,[10] with more recent studies applying DNA or even circularly-polarized light to these systems, yielding a host of novel structures with interesting optical properties.[11] These processes, which enable new approaches to control the structure of nanomaterials,[12–15] crucially depend on the inherent properties of the inorganic crystals, such as the crystal lattice,[9] stabilization of certain chiral kinks,[2] or the presence of crystalline defects such as screw dislocations.[10] In the case of Au nanocrystals, a few synthetic strategies for chirality transfer have been successfully applied, including: removing mirror planes from the geometry of achiral nanoparticle seeds in the presence of small chiral molecules such as amino acids (chemically-induced);[4] using chiral micelles to wrap around nanocrystal seeds and template further growth (micelle-directed);[16] and irradiation of nanocrystal seeds by circularly polarized light to induce asymmetric hot spots and thereby favor chiral growth (CPL-induced).[17–18] In all

[*] K. Van Gordon,[+] F. Bevilacqua, Prof. L. M. Liz-Marzán
CIC biomaGUNE, Basque Research and Technology Alliance (BRTA)
20014 Donostia-San Sebastián, Spain
E-mail: llizmarzan@cicbiomagune.es

K. Van Gordon,[+] F. Bevilacqua
Department of Applied Chemistry
University of the Basque Country (UPV-EHU)
20018 Donostia-San Sebastián, Spain

Dr. B. Ni[+]
Physical Chemistry, University of Konstanz, 78457 Konstanz, Germany
and
Present address: Department of Chemical Engineering, University of Michigan, MI 48109-2102 Ann Arbor, USA

Dr. R. Girod,[+] Dr. M. Mychinko, Prof. S. Bals
EMAT and NANOlab Center of Excellence
University of Antwerp
B-2020 Antwerp, Belgium
E-mail: sara.bals@uantwerpen.be

Prof. L. M. Liz-Marzán
Ikerbasque, Basque Foundation for Science
48009 Bilbao, Spain

Prof. L. M. Liz-Marzán
Biomedical Research Networking Center, Bioengineering, Biomaterials and Nanomedicine, CIBER-BBN
20014 Donostia-San Sebastián, Spain

Prof. L. M. Liz-Marzán
Cinbio, Universidade de Vigo
36310, Vigo, Spain

[+] These authors contributed equally to the work.

cases, the crystal properties of the achiral seeds have been reported to influence the morphology and handedness of the final chiral products. For example, Nam and colleagues obtained helicoid particles with 432 symmetry from cubic or octahedral seeds.[4,19] However, comparison of the optical response from helicoids obtained with the same amino acid enantiomer was opposite in both cases, as indicated by the sign of the bands in circular dichroism (CD) spectra.[20] Although the mechanisms related to such geometrical and optical differences remain largely unknown, it is quite clear that morphological/crystalline details in the seeds play a crucial role during crystal growth. From the reported observations, it remains unclear whether it is the seed morphology or other structural aspects, like the crystalline index of surface facets, the presence of twin boundaries, or other crystalline defects, that determine the resulting chiral morphology.

In this context, Au nanorods (NRs) are a particularly interesting system, not only because of their well-defined crystallinity, but also because differences in certain synthetic details are known to lead to crucial differences in geometrical and crystalline features. It is well known that the choice of single-crystalline (SC) or penta-twinned (PT) Au nanocrystal seeds determines the growth of either single-crystal Au NRs (grown from SC seeds in the presence of Ag^+ ions) with an octagonal cross section, or pentagonal prisms (from PT seeds and Ag-free).[21] Consequently, the crystallographic surface facets for both Au NR types are different, with SC–Au NRs displaying {520} lateral facets capped by {110} and {100} tips[22–23] and PT–Au NRs yielding {100} sides and {111} tip facets.[24] The symmetry corresponding to the morphology of a SC–Au NR is described by the 4/mmm point group, whereas for a PT–Au NR it corresponds to the $(\overline{1}0)m2$ point group (Figure S1). Since chiral growth in the presence of small chiral inducers depends on the type of crystal facet exposed at the surface of the seed,[25] we hypothesized that the use of PT–Au NRs *vs.* SC–Au NRs would lead to different chiral morphologies and potentially different optical activity.

Therefore, achiral SC- and PT–Au NR seeds with similar sizes (Figure S2) were subjected to both the chemically-induced[26] and the micelle-directed[16] chiral growth approaches. Given the different morphological features (twisted *vs.* wrinkled) that lead to chiroptical activity in each of these methods, the effects of varying the crystal habit from SC to PT were also expected to be significantly different. As previously reported, the complex morphological details of chiral Au NRs require high resolution characterization in three dimensions (3D) that could only be achieved by means of state-of-the-art electron tomography methods, which also allow quantification of the chiral structure at the nm scale.[27] Correlation between morphological and optical features is not straightforward, but the handedness of chiral structures within twisted or wrinkled nanocrystals are expected to correlate with the sign of CD bands in the corresponding spectra.[28]

Results and Discussion

The first step in the preparation of rod-like chiral particles comprises the synthesis of monodisperse SC- and PT–Au NRs. Among various methods in the literature, we selected those recently reported by us, which provide high quality and reliability. In both cases, a high aspect ratio was sought because it was found in previous work to be more efficient in terms of chiral NR growth and optical activity. In the case of SC–Au NRs, the use of small NRs (minirods) as seeds has been shown to provide access to a wider range of SC–Au NR dimensions and thus high aspect ratios can be achieved without sacrificing monodispersity.[29] For PT–Au NRs, thermal treatment of the initial seeds is effective toward enriching the population of PT nanocrystal seeds, which in turn leads to a much higher yield during seeded growth.[30] It should be noted however, that a small fraction of quasi-spherical particles may remain in the PT–Au NR dispersion (Figure S2e).

We initially explored the chemically-induced protocol, using *L*-cystine (*L*-2cys) as the chiral inducer. *L*-cystine is a dimer formed upon oxidation of the amino acid *L*-cysteine, which we found to lead to more reproducible results than the monomer, for chiral growth experiments. From our previous work,[26] we learnt that multistep seeded growth leads to better-defined twisted morphologies than those obtained when the total amount of growth solution would be added in a single step. Therefore, we implemented a multi-step protocol, including nine chiral growth steps, using both SC- and PT–Au NR seeds. The linear optical spectra of the respective final products (Figure 1a) reveal significant differences. Two well-defined extinction bands of similar intensity, centered at 591 nm and 754 nm, were recorded for the particles obtained from SC–Au NRs, whereas growth on PT–Au NRs led to a double band at shorter wavelengths (ranging from *ca.* 550 to 750 nm) and an intense band around 1050 nm. Even more remarkable are the differences observed in the corresponding CD spectra (normalized to the *g*-factor), where the bands for SC- and PT–Au NRs seem to be inverted (opposite sign) and shifted: an intense negative peak at 590 nm (maximum *g*-factor of −0.036) and a positive plateau at longer wavelengths for SC–Au NRs, but a weak negative peak at 535 nm and a more intense positive band centered at 660 nm (peak *g*-factor value of 0.020) for the product from growth on PT–Au NRs (Figure 1b). A notable observation here is that, even though seeded growth was carried out in the presence of the same (*L*-2cys) chiral inducer enantiomer, the sign of CD bands was inverted for NRs evolving from SC- and PT–Au NRs. Marked differences were also observed through electron microscopy and tomography characterization. As previously reported, chiral particles grown from SC–Au NRs (in the presence of *L*-2cys) showed a right-handed 4-fold twisted structure (Figures 1c,e and S3, S4), in agreement with the removal of mirror planes by *L*-2cys.[26] However, when growing PT–Au NRs under similar conditions, much more intricate structures were obtained (Figures 1d,f and S5), often containing cavities within

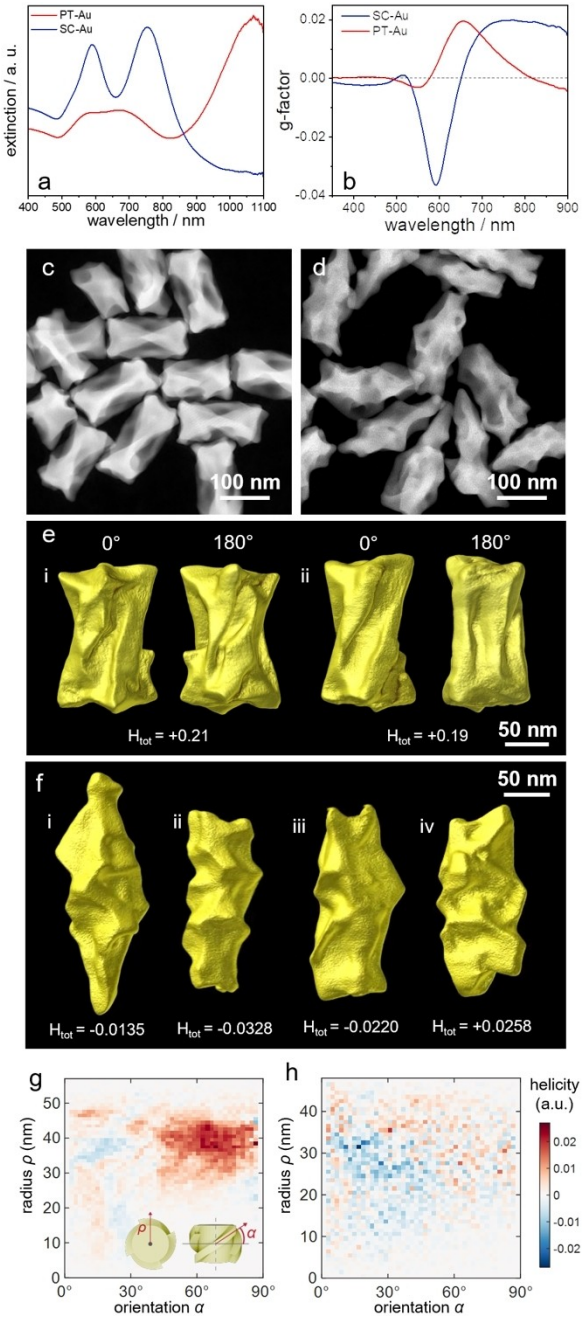

Figure 1. Characterization of chiral products using *L*-2cys as the chiral inducer. (a,b) Extinction and *g*-factor spectra for the chiral particles obtained from SC- and PT-AuNR seeds, using an identical multi-step protocol. (c,d) Representative high angle annular dark field scanning transmission electron microscopy (HAADF STEM) images of chiral SC–Au NRs (c) and PT–Au NRs (d). (e,f) Isosurface renderings of electron tomography reconstructions for typical chiral SC–Au NRs (e) and PT–Au NRs (f). Two particles are shown in e at two different orientations (0° and 180°), revealing a 4-fold symmetry. The total helicity value (H_{tot}) is indicated for each particle. (g,h) Helicity plots for the particles shown in e–i (g) and in f-ii (h). Insets in g show the definition of the orientation α and of the radius ρ (distance from central rotation axis) for a simple helix. Red dots indicate dominantly right-handed features, blue dots indicate dominantly left-handed features, the intensity scales with the number of similarly oriented surface elements (see Materials and Methods in the SI).

highly twisted surfaces, somewhat resembling the shape of a conch shell.[31–32] Along with differences in size (length of PT–Au NRs: 179.5 ± 20.1 nm *vs.* 109.2 ± 7.5 nm for SC–Au NRs), these major morphological differences are likely responsible for the observed discrepancies in the extinction spectra. These images also demonstrate strong interparticle variability within the same batch, which hinders the interpretation of the growth process. It should be noted that, even if at a lower extent of complexity, similar results were obtained when a single-step growth protocol was employed (see description in the Supporting Information and Figure S6).

To further probe the morphology of these particles and the relationship to their chiroptical properties, we conducted helicity analysis through a method specifically designed to quantify the handedness of surface features in electron tomography reconstructions.[27] The resulting helicity plots (Figure 1g,h and methods for computational details in the SI) show the histogram of right-handed (positive helicity values) or left-handed (negative helicity values) surface elements, their orientation angle (α, X-axis) and their distance from the central rotation axis of the particle (radius ρ, Y-axis). As shown in Figures 1g and S4, twisted SC–Au NRs had mostly right-handed features and positive helicity values, as previously reported.[26] In contrast, particles grown from PT–Au NRs systematically showed a mixture of right- and left-handed orientations, reflecting their complex and varied features (Figures 1h and S5). The mixed (right- and left-handed) orientations of chiral features in PT–Au NRs, combined with the greater polydispersity of the initial (PT NR) seeds, are likely to contribute to the lower *g*-factor recorded for these particles.

To investigate a possible cause of the inverted CD spectra, we further calculated the total helicity (H_{tot}) by integrating the helicity plots. This metric quantifies how close to a perfect helix a given geometry is, with the ideal case having a helicity of ± 1, depending on handedness. We systematically obtained small values for PT-derived particles (Figure 1f), typically in a range of ± 0.03. With six particles reconstructed from this sample, the averaged total helicity was -0.0127 ± 0.0480, again showing strong interparticle variability. It is therefore difficult, due to the limited sample size and despite the negative sign of the average value, to attribute a dominant morphological handedness to the PT–Au NRs and to explain the sign of the CD spectra based on this analysis. Interestingly, this also suggests that the nature of chirality in SC- and PT–Au NRs is fundamentally different, with PT–Au NRs corresponding to particles with a poorly defined structural helicity and nonobvious morphological handedness, despite their clear chiroptical properties.

Given the unexpected morphology obtained from chiral growth using PT–Au NRs, we tracked the morphological evolution upon various additions of growth solution (Figures S7 and S8). Electron tomography and helicity analysis revealed a considerably roughened surface with numerous left- and right-handed features, already after the first chiral growth step (Figure S8a,b). After 9 dissymmet-

ric growth steps, the surface exhibited even more pronounced irregularities. Overall, these results show that, at any stage of growth, the use of PT–Au NR seeds leads to roughened surfaces with both left- and right-handed tilted ridges. These observations are significantly different compared to growth starting from SC–Au NR seeds, where smooth surfaces can be identified at early stages and well-defined handedness is observed in the final stage.[26]

When using SC–Au NR seeds, cysteine-mediated chiral growth has been reported to proceed via a facet-driven mechanism, in which {521} chiral facets are formed in the presence of chirality-inducing molecules of matching handedness.[26] To assess if this mechanism also applies to PT–Au NR seeds, we conducted atomic resolution tomography on a PT–Au NR after the first growth step (Figure S9). Although the obtained reconstruction allowed us to identify crystallographic orientations (Figure S9c), indexing the surface proved difficult because of its continuously varying curvature. This observation shows that PT-based particles have less well-defined surface facets than their SC counterparts. Close inspection of the images also revealed that the five-fold twinning of the Au NR seed was preserved in the overgrown particle (Figure S9b,c), even though the C5 morphological symmetry was not.

The above results suggest that, chiral growth using PT–Au NR seeds yields chiral nanostructures with opposite optical handedness to that for chiral NRs grown from SC–Au NR seeds. However, the wide variety of morphologies obtained using PT–Au NR seeds, largely complicates the analysis and discussion of this observation. The inverted CD signal may arise from a predominance of optically-active left-handed features that helicity cannot account for, i.e. a weakly helical yet chiral morphology.[33] This type of chirality might be revealed using a measure of asymmetry such as the Hausdorff distance between a particle and its mirror image.[17]

Next, we proceeded to perform a similar study based on the alternative, micelle-induced chiral growth method, using 1,1'-binaphthyl-2,2-diamine (BINAMINE) as the chiral co-surfactant, together with cetyltrimethylammonium chloride (CTAC) as surfactant. The mechanism behind micelle-induced chiral growth is considered to involve the formation of helical micelles around the Au NR seed, subsequently templating the growth of quasi-helical features.[16] Detailed helicity analysis in previous works revealed the complexity of such surface features, containing both left- and right-handed helical wrinkles at the nm scale. However, one handedness was consistently found to dominate, in agreement with the handedness of the chiral co-surfactant used in the synthesis.[27] In this context, we hypothesized that the growth on PT- rather than SC–Au NR seeds under identical conditions might also lead to an inversion in optical activity and in the predominant wrinkle handedness. Characterization of the obtained chiral products revealed similar extinction spectra and wrinkled morphologies (see Figure 2 for *S*-BINAMINE and Figure S10 for *R*-BINAMINE), regardless of the crystallinity of the achiral Au NR seed employed in

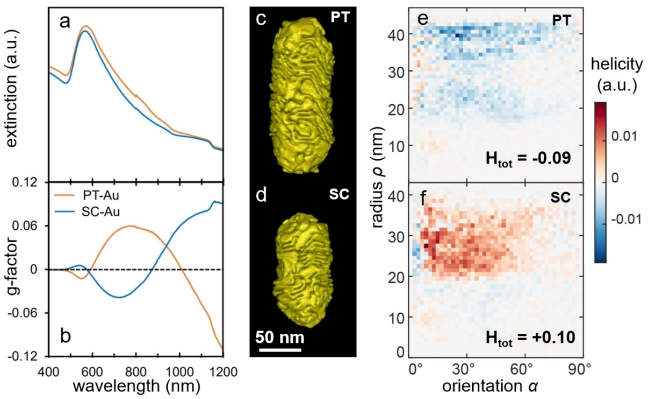

Figure 2. Characterization of chiral wrinkled Au NRs synthesized using pentatwinned or single-crystal achiral seeds, in the presence of S-BINAMINE/CTAC mixtures. (a,b) Extinction (a) and chiroptical (b) spectra of chiral nanoparticles in aqueous colloidal dispersions. (c,d) Isosurface rendering from electron tomography reconstructions of a representative PT–Au NR (c) and a SC–Au NR (d). Scale bar is valid for both images. (e, f) helicity characterization of the particles in (c) and (d), respectively.

the synthesis. Extinction spectra for both chiral products feature a band peaking at 570 nm, which tails off into the NIR region (Figures 2a and S10a). However, the chiroptical (CD/*g*-factor) signature of NRs grown from PT–Au NR seeds was found to be nearly perfectly inverted (Figures 2b and S10b). In contrast to the observations for chiral Au NRs grown using *L*-2cys, electron tomography reconstructions for several NRs grown from PT- and SC–Au NR seeds consistently revealed features of opposite morphological handedness for both samples (Figures 2c,d and S11). Even though *S*-BINAMINE was used in both syntheses as the chiral inducer, wrinkled SC–Au NRs exhibited preferentially right-handed helicity, whereas wrinkles grown on PT–Au NRs were preferentially tilting to the left. Quantification provided by helicity calculations (Figure 2e,f) confirmed this observation, yielding a total helicity of −0.09 for wrinkled PT–Au NRs, i.e., an overall left-handed helical structure, whereas a total helicity of +0.10 was determined for wrinkled SC–Au NRs, as expected for a right-handed structure.

Detailed analysis of selected reconstructions revealed additional differences in the morphologies of wrinkled Au NRs obtained from SC- and PT-achiral seeds. Whereas the latter particles typically featured blunt tips (Figure S11a,c), SC–Au NRs typically contained well-defined wrinkles, suggesting an influence of either the tip morphology or the type of crystal surface facets at the tips, on micelle adsorption and further growth. Notable differences were also found between wrinkles growing on the side facets of PT- or SC–Au NR seeds. For clarity, we first establish two definitions to describe the geometry of wrinkles on rods, as modelled in Figure S12: a wrinkle direction angle describes the angle of that wrinkle when visualized sideways or in cross-section (e.g. Figure 3a,e); a wrinkle orientation angle describes the angle of that wrinkle when visualized in a front view through isosurface rending (e.g.

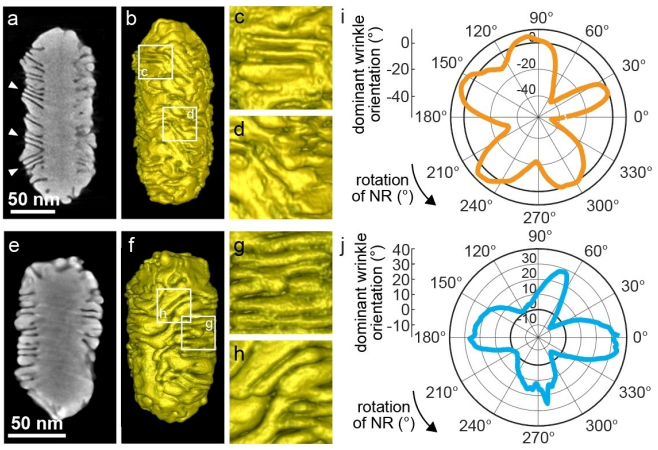

Figure 3. Morphology of wrinkles on chiral particles grown from PT- and SC–Au NRs using the micelle-templated synthesis with *S*-BINAMINE. (a–d) Central orthoslice (a) showing the direction of growth (white arrows) and isosurface visualization of the 3D reconstruction (b) of a wrinkled PT–Au NR, with close-up views of the surface (c,d) demonstrating two main orientations of the wrinkles. (e–h) Central orthoslice (e) and surface visualization (f) of a wrinkled SC–Au NR with close-up surface views (g,h). (i,j) Polar plots of the dominant wrinkle orientation in the particles shown in (b) and (f), respectively, as a function of the rotation of each particle around its major axis.

Figure 3b,f). On PT seeds, numerous wrinkles were seen to have a ±25–30° direction angle with respect to the normal direction of the surface (Figure 3a). In contrast, most of the wrinkles on SC seeds were almost perpendicular to the lateral facets, occasionally with small but random direction angles (Figure 3e). Apart from the growth direction, wrinkles were also observed to have different orientations (Figure 3b,f). Specifically, two types of areas could be distinguished on the surfaces of wrinkled particles, in which wrinkles were either mostly flat (Figure 3c,g), or mostly tilted (Figure 3d,h). To understand the distribution of these areas at the chiral NR surface, we tracked them by measuring the dominant wrinkle orientation when the NR was rotated about its major axis (see Materials and Methods and Figure S13). As shown in Figures 3i and S11d, when rotating particles grown from PT-seeds, five areas were observed to contain mainly flat wrinkles (dominant orientation close to 0°), whereas five areas had wrinkles tilting to the left (negative orientation angle). An idealized view of this geometry is presented in Figure S14. Remarkably, these areas alternated, in agreement with the 5-fold symmetry of the achiral PT seeds being preserved. Particles grown from SC seeds also contained distinct areas of flat or tilted wrinkles (albeit with positive orientation angles, i.e., to the right), but in this case with a 4-fold rotational symmetry around the major axis of the NRs (Figures 3j and S11). This symmetry is directly reminiscent of the intermediate morphologies that were reported to occur during achiral-to-chiral transitions, comprising a square cross-section with {110} facets.[26] Given the different geometries (number of faces and corners or angles at corners) and surface facets between PT seeds and SC intermediates, our observations at the tips and sides of the wrinkled Au NRs strongly suggest that such geometrical and crystallographic considerations influence the growth of wrinkles and/or micelle adsorption.

These observations hint at a possible factor to explain the CD sign and morphological handedness reversal in the micelle-directed synthetic pathway, but, as with the *L*-2cys induced synthesis, other effects may co-exist. These effects include differences in growth kinetics, different intermediate structures, preferential interaction of the BINAMINE chiral molecules with the surface facets of these intermediates, subtle differences in tip protrusions and anisotropy, etc. The influence of tip morphology on the chiroptical signature has been explored by Liu, et al., who showed through simulations that chiroptical spectra for nanocube models with high-Miller-index chiral facets were dramatically shifted—and inverted—compared to those from nanorod models possessing similar chiral facets.[34] In summary, numerous factors may influence the morphology of Au NRs and in turn their chiroptical response. Disentangling these effects will require additional characterization and new descriptors for complex chiral structures, as well as chemical strategies to probe the growth pathway.

Conclusion

We have identified a major influence of the crystallinity of achiral seeds on the handedness of Au NRs obtained using two different chiral growth methods on both SC- and PT–Au NRs, but always using the same enantiomer of the corresponding chiral inducer. When small amino acids (the dimer *L*-2cys in this case) were used as chiral inducers, SC–Au NR seeds evolved into chiral NRs with a 4-fold twisted structure, whereas growth on PT–Au NR seeds led to more complex shapes. The overall optical handedness—as measured by CD spectroscopy—was inverted for these structures. However, although SC–Au NRs showed a twisted right-handed morphology, particles grown from PT–Au NRs did not display an obvious left-handed twist, which suggests that the origin of their chiroptical properties may lie in a different type of geometrical chirality. Regarding chiral micelle-templated growth, similar rod-like structures surrounded by helical wrinkles were obtained, regardless of seed morphology (and thus facet crystallinity). In this case, inversion of the handedness for wrinkled SC- and PT–Au NRs was more evident, both in the optical (CD band inversion) and morphological (tilt angle inversion) characterization. Electron tomography analysis also allowed us to determine 4-fold and 5-fold symmetries for wrinkled SC- and PT–Au NRs, respectively, even though seeds with similar sizes were subjected to identical growth conditions. These results reinforce the notion that wrinkle growth is not random but influenced by geometrical and/or crystallographic factors, thereby highlighting a previously neglected aspect of chiral syntheses that might be exploited to yield a host of interesting

morphologies with tunable optical properties, depending on the choice of achiral seed.

Supporting Information

The authors have cited additional references within the Supporting Information.[35–42]

Acknowledgements

Ana Sánchez-Iglesias is acknowledged for support in the synthesis of pentatwinned gold nanorods. The authors acknowledge financial support by the European Research Council (ERC CoG No. 815128 REALNANO to S.B.), from MCIN/AEI/10.13039/501100011033 (Grant PID2020-117779RB-I00 to L.M.L.-M and FPI Fellowship PRE2021-097588 to K.V.G.), and by KU Leuven (C14/22/085). This work has been funded by the European Union under Project 101131111—DELIGHT. Funding for open access charge: Universidade de Vigo/ CRUE-CISUG.

Conflict of Interest

The authors declare no conflict of interest.

Data Availability Statement

The data that support the findings of this study are available from the corresponding author upon reasonable request.

Keywords: chirality · gold nanoparticles · plasmonics · electron tomography · chiral crystal growth

[1] S. Wang, X. Liu, S. Mourdikoudis, J. Chen, W. Fu, Z. Sofer, Y. Zhang, S. Zhang, G. Zheng, *ACS Nano* **2022**, *16*, 19789–19809.
[2] C. Orme, A. Noy, A. Wierzbicki, M. McBride, M. Grantham, H. Teng, P. Dove, J. DeYoreo, *Nature* **2001**, *411*, 775–779.
[3] L. Addadi, S. Weiner, *Nature* **2001**, *411*, 753–755.
[4] H.-E. Lee, H.-Y. Ahn, J. Mun, Y. Y. Lee, M. Kim, N. H. Cho, K. Chang, W. S. Kim, J. Rho, K. T. Nam, *Nature* **2018**, *556*, 360–365.
[5] S. W. Im, H.-Y. Ahn, R. M. Kim, N. H. Cho, H. Kim, Y.-C. Lim, H.-E. Lee, K. T. Nam, *Adv. Mater.* **2020**, *32*, 1905758.
[6] S. Wang, L. Zheng, W. Chen, L. Ji, L. Zhang, W. Lu, Z. Fang, F. Guo, L. Qi, M. Liu, *CCS. Chem* **2020**, *3*, 2473–2484.
[7] S. Yang, H. Li, R. Liu, C. Wang, J. Yu, S. Li, Y. Wang, H. Chen, *Inorg. Chem. Front.* **2022**, *9*, 4136–4141.
[8] B. Ni, J. Zhou, L. Stolz, H. Cölfen, *Adv. Mater.* **2023**, *35*, 2209810.
[9] P.-P. Wang, S.-J. Yu, A. O. Govorov, M. Ouyang, *Nat. Commun.* **2017**, *8*, 14312.
[10] A. Ben-Moshe, A. da Silva, A. Müller, A. Abu-Odeh, P. Harrison, J. Waelder, F. Niroui, C. Ophus, A. M. Minor, M. Asta, W. Theis, P. Ercius, A. P. Alivisatos, *Science* **2021**, *372*, 729–733.
[11] Y. Wang, A. Tay, *ACS Nano* **2023**, *17*, 9850–9869.
[12] W. Ma, L. Xu, A. F. de Moura, X. Wu, H. Kuang, C. Xu, N. A. Kotov, *Chem. Rev.* **2017**, *117*, 8041–8093.
[13] A. Visheratina, N. A. Kotov, *CCS. Chem* **2020**, *2*, 583–604.
[14] B. Ni, H. Cölfen, *SmartMat* **2021**, *2*, 17–32.
[15] N. A. Kotov, L. M. Liz-Marzan, P. S. Weiss, *ACS Nano* **2021**, *15*, 12457–12460.
[16] G. González-Rubio, J. Mosquera, V. Kumar, A. Pedrazo-Tardajos, P. Llombart, D. M. Solís, I. Lobato, E. G. Noya, A. Guerrero-Martínez, J. M. Taboada, F. Obelleiro, L. G. MacDowell, S. Bals, L. M. Liz-Marzán, *Science* **2020**, *368*, 1472–1477.
[17] L. Xu, X. Wang, W. Wang, M. Sun, W. J. Choi, J.-Y. Kim, C. Hao, S. Li, A. Qu, M. Lu, X. Wu, F. M. Colombari, W. R. Gomes, A. L. Blanco, A. F. de Moura, X. Guo, H. Kuang, N. A. Kotov, C. Xu, *Nature* **2022**, *601*, 366–373.
[18] L. V. Besteiro, A. Movsesyan, O. Ávalos-Ovando, S. Lee, E. Cortés, M. A. Correa-Duarte, Z. M. Wang, A. O. Govorov, *Nano Lett.* **2021**, *21*, 10315–10324.
[19] H.-E. Lee, R. M. Kim, H.-Y. Ahn, Y. Y. Lee, G. H. Byun, S. W. Im, J. Mun, J. Rho, K. T. Nam, *Nat. Commun.* **2020**, *11*, 263.
[20] X. Sun, J. Yang, L. Sun, G. Yang, C. Liu, Y. Tao, Q. Cheng, C. Wang, H. Xu, Q. Zhang, *ACS Nano* **2022**, *16*, 19174–19186.
[21] M. Liu, P. Guyot-Sionnest, *J. Phys. Chem. B* **2005**, *109*, 22192–22200.
[22] B. Goris, S. Bals, W. Van den Broek, E. Carbó-Argibay, S. Gómez-Graña, L. M. Liz-Marzán, G. Van Tendeloo, *Nat. Mater.* **2012**, *11*, 930–935.
[23] E. Carbó-Argibay, B. Rodríguez-González, S. Gómez-Graña, A. Guerrero-Martínez, I. Pastoriza-Santos, J. Pérez-Juste, L. M. Liz-Marzán, *Angew. Chem. Int. Ed.* **2010**, *49*, 9397–9400.
[24] C. J. Johnson, E. Dujardin, S. A. Davis, C. J. Murphy, S. Mann, *J. Mater. Chem.* **2002**, *12*, 1765–1770.
[25] J. Morales-Vidal, N. López, M. A. Ortuño, *J. Phys. Chem. C* **2019**, *123*, 13758–13764.
[26] B. Ni, M. Mychinko, S. Gómez-Graña, J. Morales-Vidal, M. Obelleiro-Liz, W. Heyvaert, D. Vila-Liarte, X. Zhuo, W. Albrecht, G. Zheng, G. González-Rubio, J. M. Taboada, F. Obelleiro, N. López, J. Pérez-Juste, I. Pastoriza-Santos, H. Cölfen, S. Bals, L. M. Liz-Marzán, *Adv. Mater.* **2023**, *35*, 2208299.
[27] W. Heyvaert, A. Pedrazo-Tardajos, A. Kadu, N. Claes, G. González-Rubio, L. M. Liz-Marzán, W. Albrecht, S. Bals, *ACS Mater. Lett.* **2022**, *4*, 642–649.
[28] M. Obelleiro-Liz, V. F. Martín, D. M. Solís, J. M. Taboada, F. Obelleiro, L. M. Liz-Marzán, *Adv. Opt. Mater.* **2023**, *11*, 2203090.
[29] G. González-Rubio, V. Kumar, P. Llombart, P. Díaz-Núñez, E. Bladt, T. Altantzis, S. Bals, O. Peña-Rodríguez, E. G. Noya, L. G. MacDowell, A. Guerrero-Martínez, L. M. Liz-Marzán, *ACS Nano* **2019**, *13*, 4424–4435.
[30] A. Sánchez-Iglesias, N. Winckelmans, T. Altantzis, S. Bals, M. Grzelczak, L. M. Liz-Marzán, *J. Am. Chem. Soc.* **2017**, *139*, 107–110.
[31] P. Knoll, N. Wu, O. Steinbock, *Phys. Rev. Mater.* **2020**, *4*, 063402.
[32] W. Kunz, M. Kellermeier, *Science* **2009**, *323*, 344–345.
[33] R. B. King, *Ann. New York Acad. Sci.* **2003**, *988*, 158–170.
[34] H. Liu, A. E. Vladár, P.-P. Wang, M. Ouyang, *J. Am. Chem. Soc.* **2023**, *145*, 7495–7503.
[35] M. Odstrčil, M. Holler, J. Raabe, M. Guizar-Sicairos, *Opt. Express* **2019**, *27*, 36637–36652.
[36] T. Altantzis, I. Lobato, A. De Backer, A. Béché, Y. Zhang, S. Basak, M. Porcu, Q. Xu, A. Sánchez-Iglesias, L. M. Liz-Marzán, G. Van Tendeloo, S. Van Aert, S. Bals, *Nano Lett.* **2019**, *19*, 477–481.

[37] W. van Aarle, W. J. Palenstijn, J. De Beenhouwer, T. Altantzis, S. Bals, K. J. Batenburg, J. Sijbers, *Ultramicroscopy* **2015**, *157*, 35–47.
[38] W. van Aarle, W. J. Palenstijn, J. Cant, E. Janssens, F. Bleichrodt, A. Dabravolski, J. De Beenhouwer, K. Joost Batenburg, J. Sijbers, *Opt. Express* **2016**, *24*, 25129–25147.
[39] J. Sa, N. Hu, W. Heyvaert, K. Van Gordon, H. Li, L. Wang, S. Bals, L. M. Liz-Marzán, W. Ni, *Chem. Mater.* **2023**, *35*, 6782–6789.
[40] R. Rezakhaniha, A. Agianniotis, J. T. C. Schrauwen, A. Griffa, D. Sage, C. V. C. Bouten, F. N. van de Vosse, M. Unser, N. Stergiopulos, *Biomech. Model. Mechanobiol.* **2012**, *11*, 461–473.
[41] E. Fonck, G. G. Feigl, J. Fasel, D. Sage, M. Unser, D. A. Rüfenacht, N. Stergiopulos, *Stroke* **2009**, *40*, 2552–2556.
[42] Z. Püspöki, M. Storath, D. Sage, M. Unser, in: W. De Vos, S. Munck, J. P. Timmermans (eds) *Focus on Bio-Image Informatics. Advances in Anatomy*, *Embryology and Cell Biology*, vol 219 (2016). Springer, Cham.

Manuscript received: February 13, 2024
Accepted manuscript online: April 22, 2024
Version of record online: ■■, ■■

Research Articles

Nanocrystals

K. Van Gordon, B. Ni, R. Girod, M. Mychinko, F. Bevilacqua, S. Bals,* L. M. Liz-Marzán* _____ **e202403116**

Single Crystal and Pentatwinned Gold Nanorods Result in Chiral Nanocrystals with Reverse Handedness

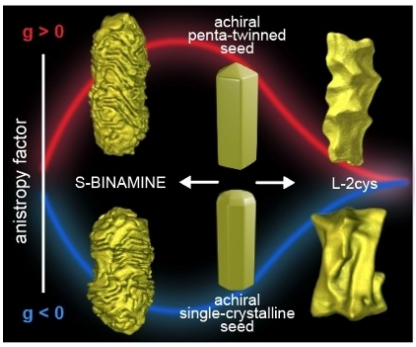

The handedness of chiral gold nanorods synthesized by seeded growth typically follows that of the organic chiral inducer, being right-handed when templated by *S*-BINAMINE micelles or induced by *L*-cystine (*L*-2cys). Our results demonstrate that a change in the achiral seed, from single crystalline to pentatwinned, can reverse the sign of circular dichroism (CD) measurements, adding a new effect to guide the chirality of gold nanoparticles.

Angewandte Chemie
Eine Zeitschrift der Gesellschaft Deutscher Chemiker

Supporting Information

Single Crystal and Pentatwinned Gold Nanorods Result in Chiral Nanocrystals with Reverse Handedness

K. Van Gordon, B. Ni, R. Girod, M. Mychinko, F. Bevilacqua, S. Bals, L. M. Liz-Marzán**

Single Crystal and Pentatwinned Gold Nanorods Result in Chiral Nanocrystals with Reverse Handedness

Kyle Van Gordon,[a,b]# Bing Ni[c]#, Robin Girod[d]#, Mikhail Mychinko[d], Francisco Bevilacqua[a,b], Sara Bals* [d], and Luis M. Liz-Marzán*[a,e,f,g]

[a] K. Van Gordon, F. Bevilacqua, Prof. L. M. Liz-Marzán
CIC biomaGUNE, Basque Research and Technology Alliance (BRTA)
Paseo de Miramón 194
20014 Donostia-San Sebastián, Spain
E-mail: llizmarzan@cicbiomagune.es

[b] K. Van Gordon, F. Bevilacqua
Department of Applied Chemistry
University of the Basque Country (UPV-EHU)
20018 Donostia-San Sebastián, Spain

[c] Dr. B. Ni
Physical Chemistry, University of Konstanz, 78457 Konstanz, Germany
Present address: Department of Chemical Engineering, University of Michigan, MI 48109-2102 Ann Arbor, USA

[d] Dr. R. Girod, Dr. M. Mychinko, Prof. S. Bals
EMAT and NANOlab Center of Excellence
University of Antwerp
B-2020 Antwerp, Belgium
E-mail: sara.bals@uantwerpen.be

[e] Prof. L. M. Liz-Marzán
Ikerbasque, Basque Foundation for Science
48009 Bilbao, Spain

[f] Prof. L. M. Liz-Marzán
Biomedical Research Networking Center, Bioengineering, Biomaterials and Nanomedicine, CIBER-BBN
20014 Donostia-San Sebastián, Spain

[g] Prof. L. M. Liz-Marzán
Cinbio, Universidade de Vigo36310, Vigo, Spain

# These authors contributed equally to the work

* Corresponding authors

Materials and Methods

Chemicals: $HAuCl_4 \cdot 3H_2O$ (99.99% (metals basis)), and *L*-Cystine hydrochloride (*L*-2cys, 98%) were purchased from Alfa Aesar. Ascorbic acid (AA) was purchased from Acros Organics. $AgNO_3$ (>99.9%) was purchased from Roth. (*R*)-(+)-1,1'-binaphthyl-2,2'-diamine (*R*-BINAMINE, 99%), (*S*)-(−)-1,1'-binaphthyl-2,2'-diamine (*S*-BINAMINE, 99%), cetyltrimetryammonium chloride (CTAC, >98.0%), cetyltrimethylammonium bromide (CTAB; 99%), silver nitrate ($AgNO_3$; ≥ 99.0%), n-decanol (for synthesis; ≥ 99.0%), sodium borohydride ($NaBH_4$; 99%), and ascorbic acid (AA; ≥ 99%) were all purchased from Sigma-Aldrich. Hydrochloric acid (HCl; ACS, ISO grade, 3% w/v) was sourced from Scharlau. All reagents were used as received without further purification. Milli Q water was used to prepare solutions.

Synthesis of pentatwinned Au nanorods (PT-Au NRs): Pentatwinned nanorods were synthesized using a method adopted from the literature.[30] In general, a two-step synthesis involving the preparation of twinned Au seeds and larger rods was implemented. To prepare pentatwinned Au seeds, a 0.05 M $HAuCl_4$ solution (50 µL) was added to 10 mL of 50 mM CTAC and 5 mM citric acid. After 30 minutes, a solution of a 25 mM $NaBH_4$ solution (250 µL) was quickly added to the mixture. After a further 2 minutes, the seeds are aged for 90 min at 80 ºC with stirring to encourage twinning. For nanorod growth, a 0.05 M $HAuCl_4$ solution (125 µL) was mixed with 50 mL of 8 mM CTAB. The mixture was stored at 20 °C for at least 15 minutes, to allow for complete complexation between the Au^{3+} and CTAB. After this time, a 0.1 M solution of AA (125 µL) was added, followed by 100 µL of pentatwinned Au seeds (Au^{3+}/Au = 1.25). The reaction mixture was left undisturbed overnight, and then centrifuged at 3000 rpm for 10 min and washed with 10 mM CTAC thrice.

Synthesis of single-crystalline Au nanorods (SC-Au NRs): Single-crystalline nanorods were synthesized using a method adopted from the literature.[29] In brief, a three-step synthesis involving the preparation of Au cluster seeds, mini rods, and larger rods was implemented. To prepare the Au cluster seeds, a 0.05 M $HAuCl_4$ solution (200 µL) and 100 µL of a 0.1 M AA solution were added to 20 mL of a 50 mM CTAB and 13.5 mM *n*-decanol solution, in a 50 mL glass beaker at 25−27 °C. A colorless solution was obtained. After 1−2 min, 800 µL of a freshly prepared 0.02 M $NaBH_4$ solution was injected under vigorous stirring. Excess borohydride was consumed by aging the seed solution for at least 60 min at 25−27 °C, prior to use. Then Au mini rods were synthesized by the following protocol: 2400 µL of 0.01 M $AgNO_3$, 21 mL of 1 M HCl, 3000 µL of 0.05 M $HAuCl_4$, and 3900 µL of 0.1 M AA were added to 300 mL of a 50 mM CTAB and 13.5 mM *n*-decanol solution, at 25 °C. Then, 18 mL of the seed solution was added under stirring. The mixture was left undisturbed at 25 °C for at least 4 h. The longitudinal LSPR of the small anisotropic nanocrystals at this point should be located at 725−730 nm. The obtained small anisotropic seeds were centrifuged at 14000−15000 rpm for 45−60 min. After washing, the final Au^0 concentration of Au mini rods was fixed to 4.65 mM (Abs_{400nm}: 1, optical path of 1 mm). Larger SC-Au NRs were then synthesized by the following steps: 3000 µL of 0.01 M $AgNO_3$, 1000 µL of 0.05 M $HAuCl_4$, 800 µL of 0.1 M AA, and a certain amount of 1M HCl solution were added to 100 mL of a 50 mM CTAB and 11 mM *n*-decanol solution. After vigorous stirring, 500 µL of the Au mini rods was added into the mixture and stirred. The mixture was then left undisturbed at 35 °C for at least 4 h, and subsequently centrifuged at 8000 rpm for 15 min and washed with 10 mM CTAB solutions.

Chiral growth of PT-Au NRs and SC-Au NRs: The methods were adopted from the literature.[16,26] The multi-step synthesis protocol is described in the following: the concentration of PT-Au NRs and SC-Au NRs was adjusted to 0.8 mM, according to the optical absorbance at 400 nm. Then 1.9 mL of CTAC solution (40 mM) was poured into a tube, followed by addition of 5 µL of $HAuCl_4$ (5 mM) and 0.2 mL of AA (0.1 M). The solution was sonicated for 30s. Then, 30 µL of *L*-2cys (2.5 µM) was added into the PE tube, followed by addition of 10 µL of seed solution, shaking several times and store in a water bath at 25 ^oC (this step is called as the first addition). After 50 min, 5 µL of $HAuCl_4$ (5 mM) was added into the PE tube. The addition was repeated several times, and the temperature of the water bath could also be tuned according to the growth requirements. After the 6 $HAuCl_4$ addition steps, the temperature of the water bath was decreased to 16 ^oC. After 9 additions, the PE tube was centrifuged (6000 rpm, 5 min) and washed twice with H_2O. The obtained particles were dispersed in H_2O. The sizes of the chiral products were significantly different when using different seeds. For the chiral particles obtained from SC-Au NRs we measured an average particle length of 109.2 ± 7.5 nm and average width of 61.4 nm ± 4.7 nm (for optical characterization) and 154.6 ± 11.5 nm x 77.9 ± 7.8 nm (for electron tomography), which depended on the size of the starting SC-Au NR. On the other hand, an average length was determined of 179.5 ± 20.1 nm for the particles obtained from PT-Au NRs, but we hesitate to indicate accurate values for their width, given their ill-defined lateral morphologies.

For chiral particles prepared using the micelle-directed strategy, single-crystal or pentatwinned achiral seeds were first incubated overnight in a chiral solution of 50 mM CTAC and 1.25 mM *R*- or *S*- BINAMINE. A typical chiral synthesis was prepared in an Eppendorf tube at a total volume of 1 mL, using 500 µM BINAMINE, 20 mM CTAC, 500 µM $HauCl_4$, 160 mM ascorbic acid, and 31.25 µM achiral seeds (Au_0). Seeds and ascorbic acid were sequentially added, and the tube was immediately shaken before leaving for 30 minutes at room temperature. Chiral particles were centrifuged at 3000 rpm for 10 minutes and resuspended in MILLIPORE-grade water. This process was repeated twice to separate chiral products from excess reagents and non-chiral reaction byproducts. The optical spectra for both SC and PT products made in this way included a single broad extinction peak around 580 nm, which trailed off into the NIR range. The obtained wrinkled rods had average dimensions of 134.4 ± 8.3 nm x 65.1 nm ± 5.6 nm for chiral SC-Au NRs, and 182.9 ± 11.2 nm x 76.2 nm ± 2.9 nm for chiral PT-Au NRs.

Characterization: A JEOL 2200FS HRTEM operated at 200 kV, was used to perform bright field and high-angle annular-dark-field (HAADF) scanning TEM (STEM). Atomic resolution HAADF-STEM images were acquired using a probe-corrected Titan Themis microscope operated at 300 kV. Tilt-series for tomography were acquired typically over ± 75° in 3° or 2^o increments for atomic resolution electron tomography measurements or conventional tomography measurements, respectively. A Cary 50 UV-Visible Spectrophotometer from Agilent Technologies, and a JASCO J-815 Circular Dichroism (CD) spectropolarimeter were used for UV-Vis and CD spectroscopy, respectively.

Electron tomography reconstructions: The tilt-series were aligned with a combination of in-house Matlab code to perform cross-correlation and using the cSAXS Matlab package to perform vertical-mass fluctuation and projection-matching alignments with sub-pixel accuracy.[35] 3D reconstructions were computed with an in-house method using a constrained version of the SIRT algorithm,[34] or with the standard expected maximization (EM) algorithm using the Astra toolbox 2.1 for Matlab.[37,38]

Helicity calculation: Helicities and helicity plots were calculated using previously established definitions and methods.[27,39] The surface of the NR was extracted by manually segmenting the tomographic reconstructions. The normal vector of the surface elements was then used to calculate the orientation (or inclination) of each element with respect to the major axis of the NR. For each NR, helicity functions $H(\alpha,\rho)$ and total helicity H_{tot} were calculated, whereby helicity is defined as the integral of orientation angles over the NR surface. We attribute a positive helicity value to surfaces with dominantly right-handed orientations and a negative helicity to surfaces with dominantly left-handed orientations. The helicity function $H(\alpha,\rho)$ is a distribution mapping a helicity value for a cylindrical section at radius ρ and surface elements of orientation α. H_{tot} integrates the entire surface at all possible orientations, resulting in a scalar value where -1 corresponds to a perfect left handed helix, +1 corresponds to a perfect right-handed helix and 0 indicates no helical character and thus no dominant orientation of the surface elements.

Dominant wrinkle orientation: To track the dominant wrinkle orientation, the 3D reconstructions were sliced to obtain tomograms going through the wrinkled corona, typically 20-30 nm away from the center of the NRs, for a range of rotation angles (see the schematized pipeline in **Figure S13**). The OrientationJ plugin for ImageJ/FIJI was then used to calculate the dominant orientation in a central subarea of these rotational tomograms. Details about the plugin can be found elsewhere.[40,41] Briefly, the dominant orientation is calculated as the angle of the first eigenvector of the gradient structure tensor matrix.[42]

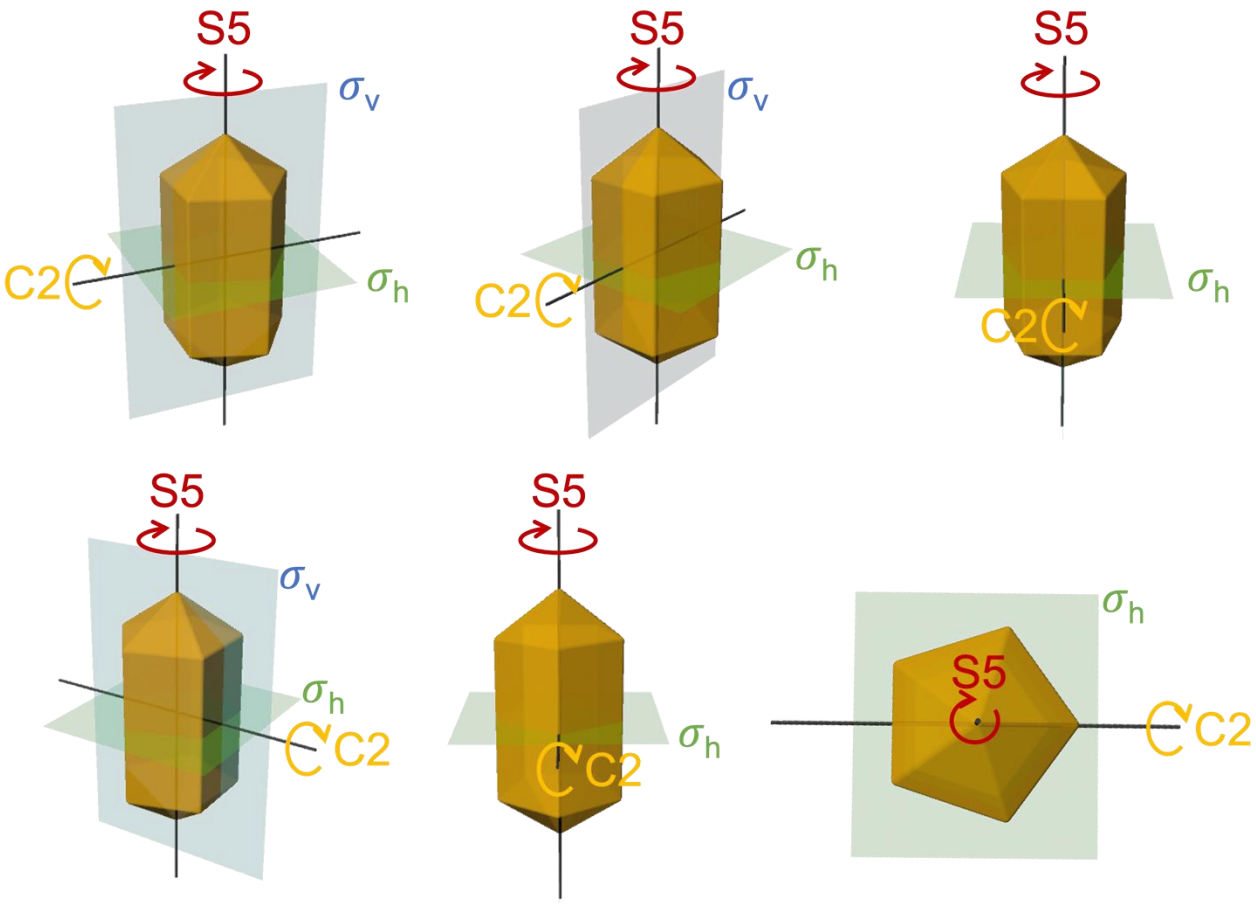

Figure S1. Main symmetry elements of a PT-Au NR along different observation angles.

Due to the existence of five twin planes, the symmetry of PT-Au NR can be very different to that in single-crystalline fcc lattices, i.e., not a subset of the $\frac{4}{m}\bar{3}\frac{2}{m}$ symmetry. The symmetry elements of a PT-Au NR contain a S5 main improper rotation axis (marked in red) with 5 perpendicular C2 axes (marked in orange), 5 vertical mirror planes (σ_v, marked in blue), and one horizontal mirror plane (σ_h, marked in green). Only one C2 axis and one vertical mirror plane (σ_v) are shown here for simplicity, the rest 4 C2 axes and 4 vertical mirror planes can be constructed according to the S5 axis. Hence, the structure belongs to the D5h point group, according to the Schoenflies notation, which is equivalent to the $(\overline{10})m2$ symmetry in the Hermann–Mauguin notation.

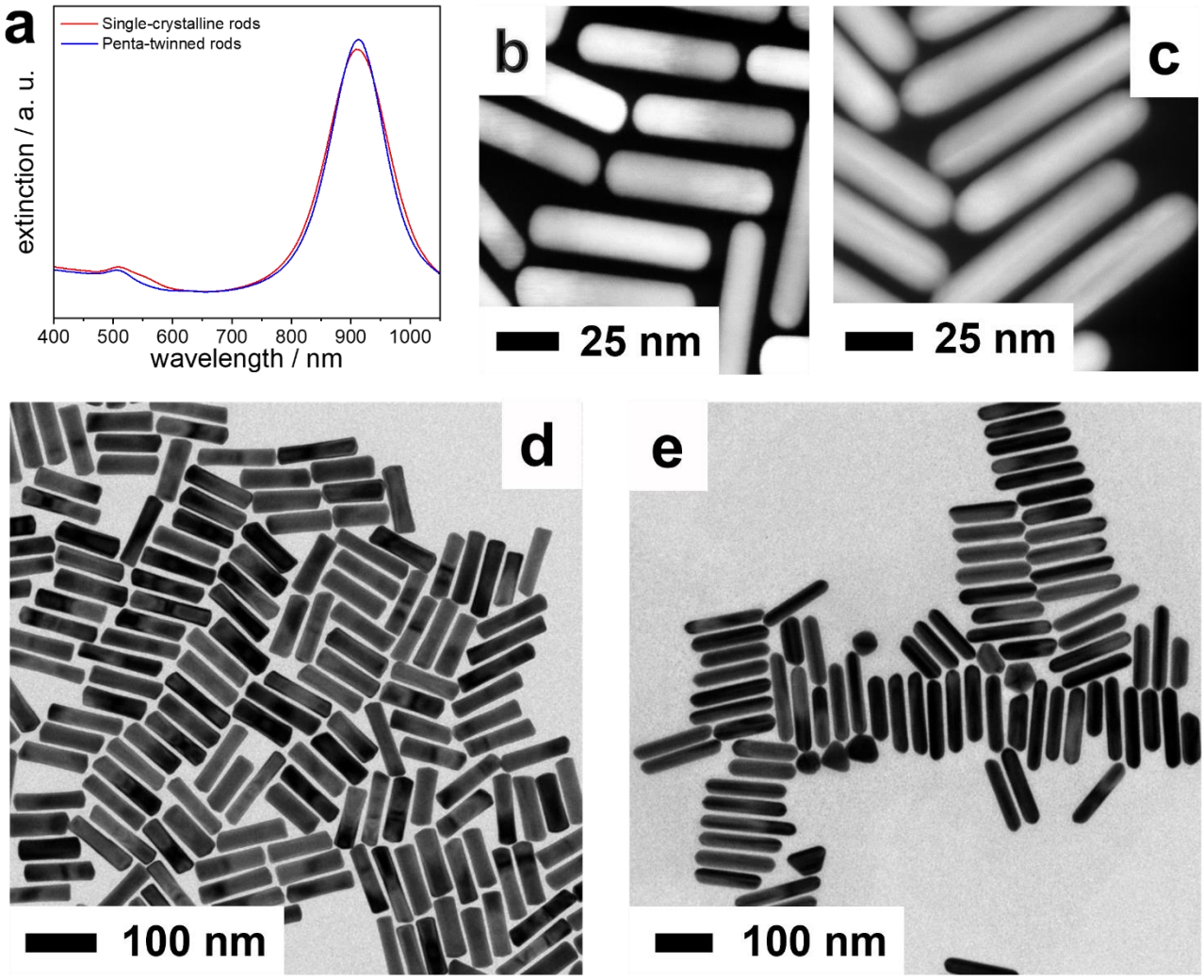

Figure S2. (a) Extinction spectra of SC- and PT-Au NR seeds used in the chemically-induced protocol; (b, c) HAADF-STEM images of SC- and PT-Au NR seeds, respectively.

The SC-Au NRs were 75.4±6.3 nm long and 15.6±1.6 nm wide (AR~4.8), whereas PT-Au NRs had dimensions of 90.9±4.2 nm in length and 19.3±1.3 nm in width (AR~4.7). (200 particles were measured, error bars indicate the standard deviation)

(d,e) TEM images of SC-Au (a) and PT-Au (b) NR seeds, respectively, used in the chiral micelle growth protocol. The SC-Au NRs were 101±17.3 nm long and 29.0±5.3 nm wide (AR~3.5), whereas PT-Au NRs had dimensions of 122±30.4 nm in length and 31.3±6.5 nm in width (AR~3.9).

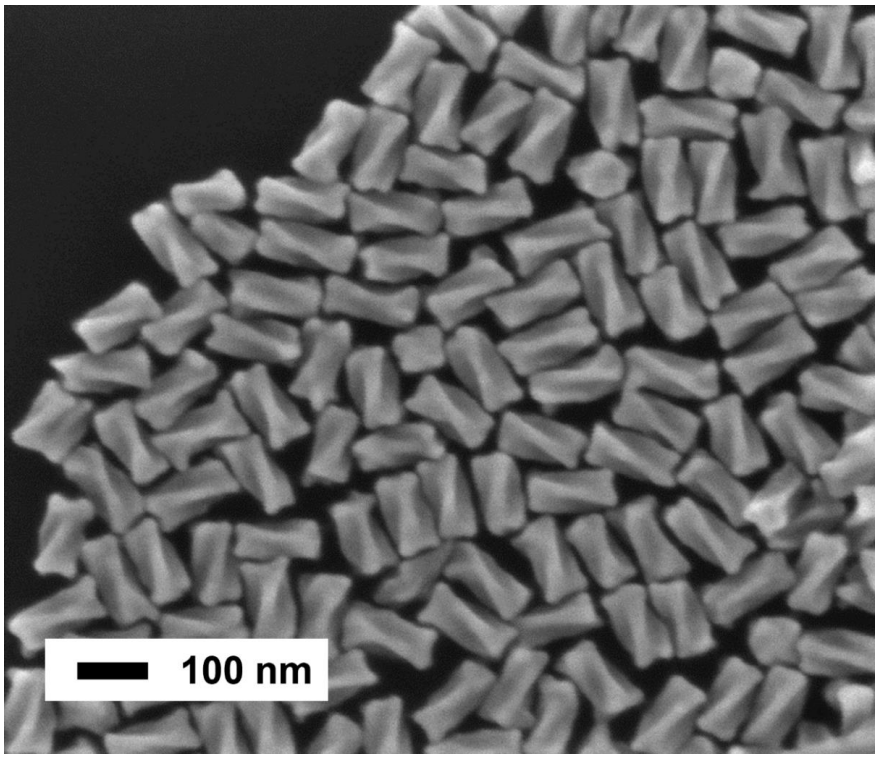

Figure S3. Representative scanning electron microscopy (SEM) image of chiral products obtained by a multi-step growth of SC-Au NRs, in the presence of *L*-2Cys. A right-handed helical structure can be easily identified.

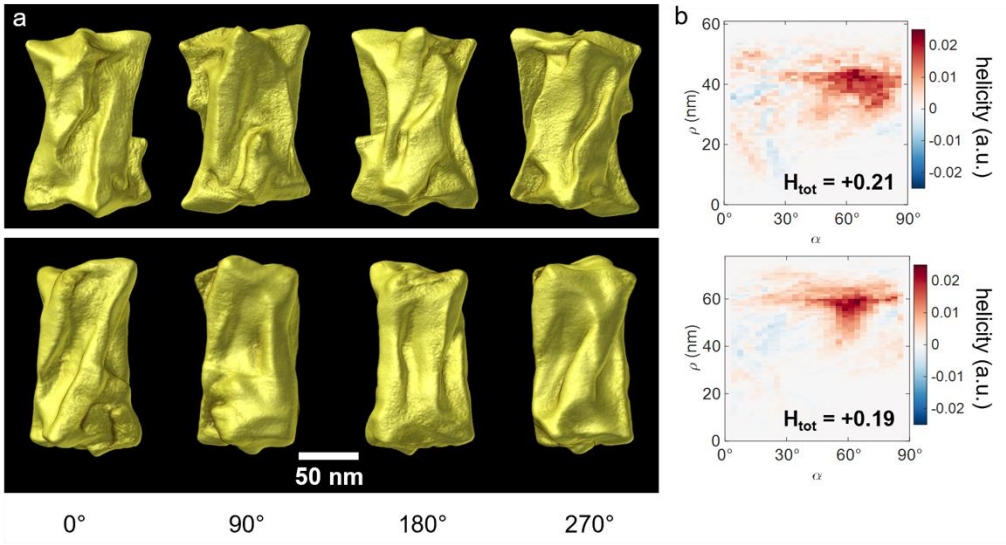

Figure S4. Electron tomography analysis of SC-Au NRs obtained by multi-step growth, in the presence of *L*-2Cys. (a) isosurface rendering of the reconstructed NRs viewed at different angles, revealing a 4-fold symmetry. (c) Helicity plot of the particles. The dominance of right-handed features is visualized by a cluster of positive helicities (red pixels).

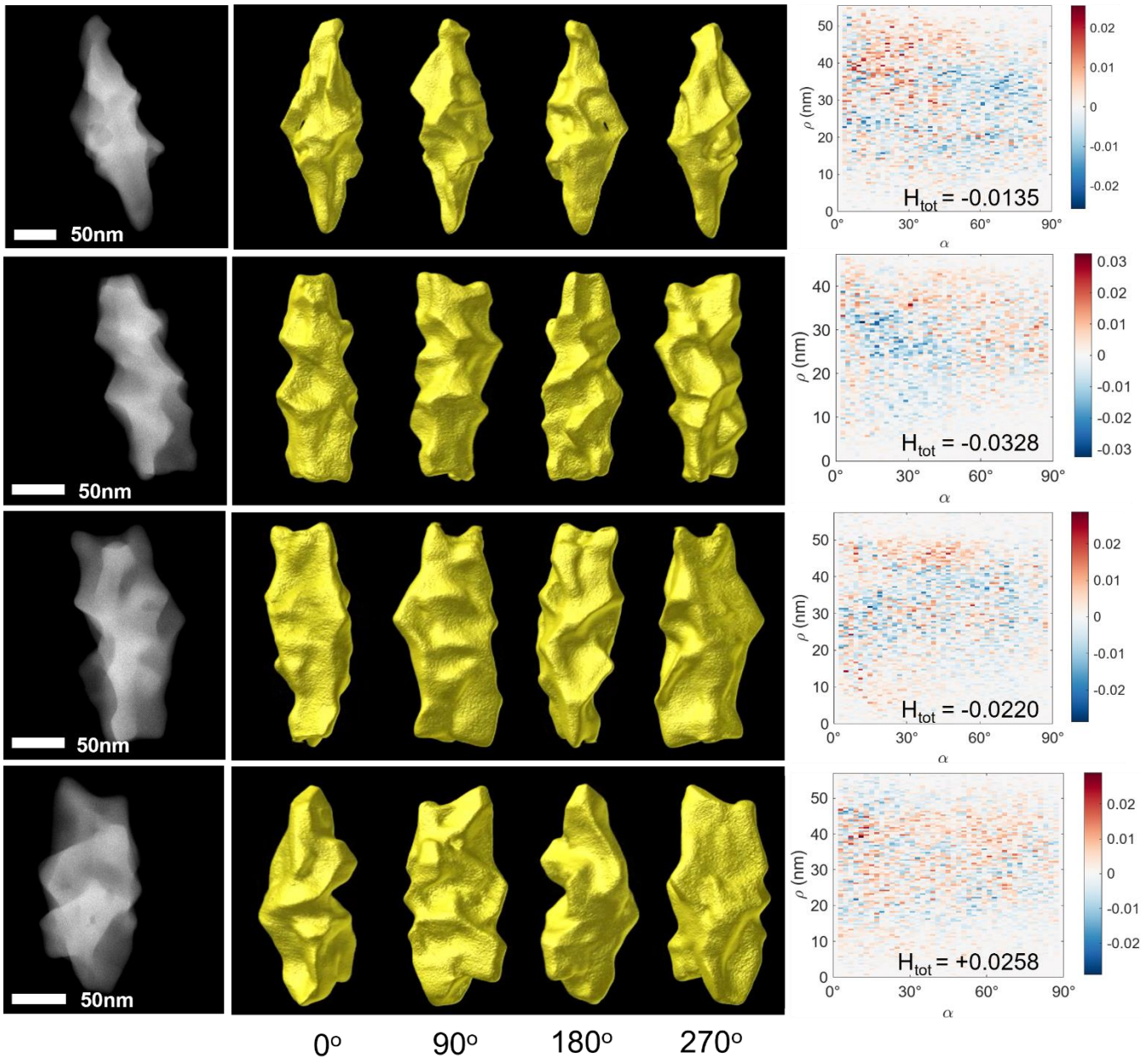

Figure S5. Isosurface visualizations of 3D reconstructions for several Au nanoparticles obtained through multi-step chiral growth. All four particles were obtained from the same synthesis batch. It can be seen that the overall morphologies differ significantly, even though all particles contain rough surfaces and tilted ridges. The corresponding helicity analysis showed both left- (blue pixels) and right-handed (red pixels) surfaces. Total helicity calculations yielded an overall left-handed helicity for most of the particles (negative H_{tot}).

Results of single-step seeded growth in the presence of *L*-2cys

Single-step growth in the presence of *L*-2Cys also resulted in remarkably different morphologies for PT- or SC-Au NRs. Whereas SC-Au NRs evolved into helical cuboid-like structures with obvious tip protrusions, PT-Au NRs evolved into complex structures. The linear optical response for both SC and PT products included an extinction peak around 580 nm (usually assigned to a transverse localized surface plasmon resonance – LSPR), whereas the second (longitudinal) LSPR band was significantly redshifted for chiral PT-Au NRs, compared to chiral SC-Au NRs, in agreement with a larger average aspect ratio for the former (PT chiral NRs: 199.8 ± 6.3 nm x 68.1 nm ± 4.0 nm; SC chiral NRs = 118.5 ± 8.6 nm x 47.0 nm ± 3.7 nm). More remarkable differences were observed in the corresponding circular dichroism (CD) spectra, which showed a negative peak at 595 nm and a positive plateau at the NIR region for chiral SC-Au NRs, whereas twisted PT-Au NRs featured a positive peak at 563 nm and a negative plateau at the NIR region.

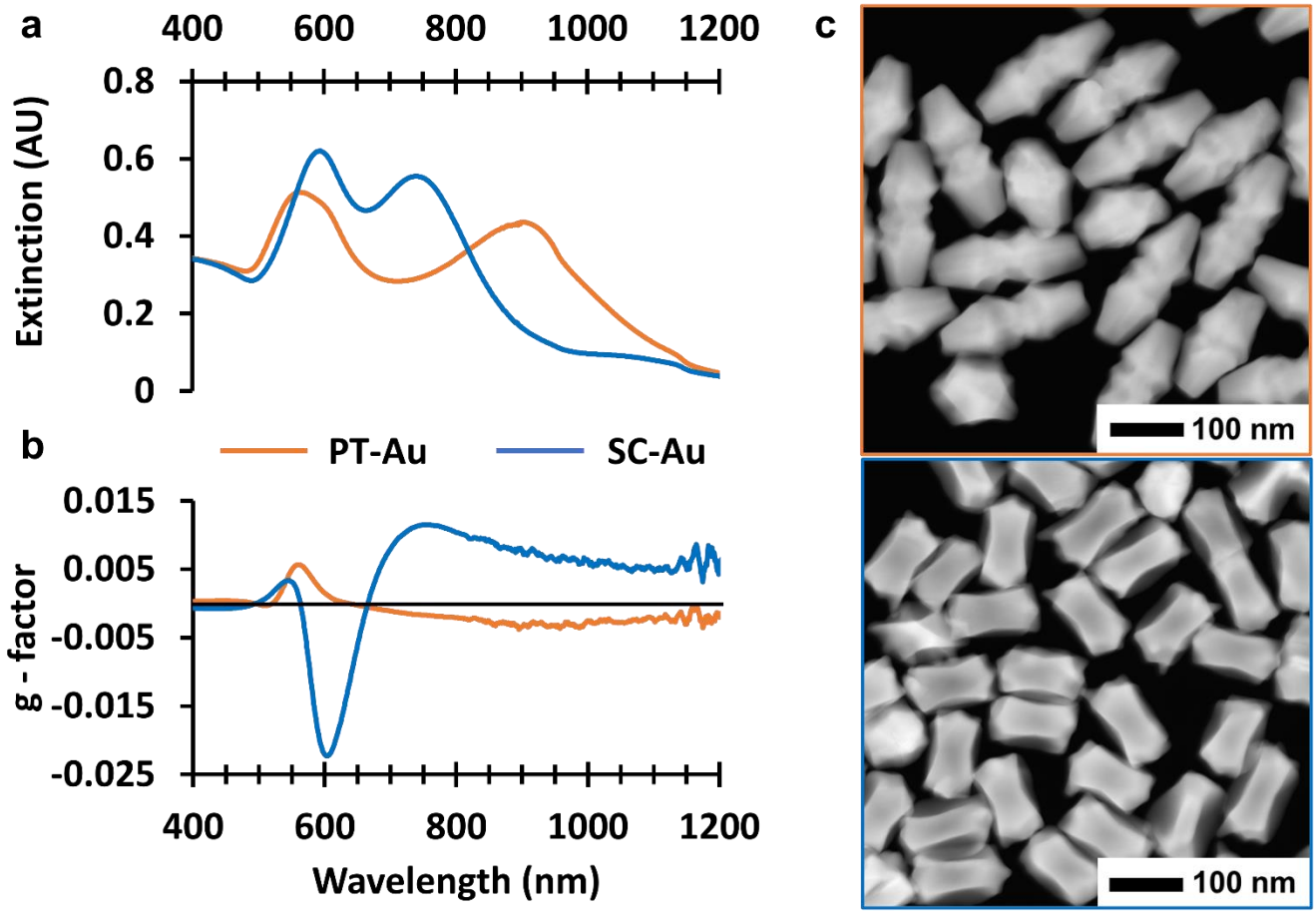

Figure S6. Extinction (a) and chiroptical spectra (b) for particles synthesized by a single-step growth protocol, using *L*-2cys and PT- or SC-NR seeds, as labeled. HAADF-STEM characterization of chiral products (c), image outlines are color-coded to match legend of plot.

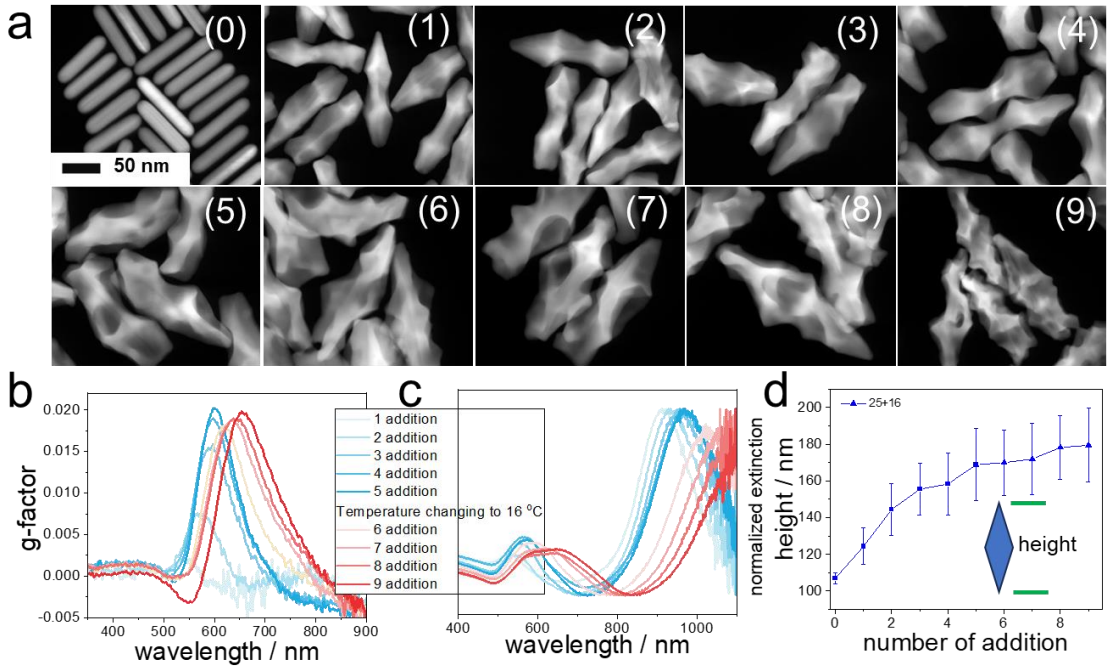

Figure S7. (a) Representative STEM images of the products obtained after different number of $HAuCl_4$ additions on PT-AuNRs (as labeled), in the presence of *L*-2cys. The scale bar applies to all images. (b,c) Corresponding *g*-factor and extinction spectra during the various growth steps. (d) Particle height (as defined in the inset) as a function of the number of $HAuCl_4$ additions. The particle length was measured on 300 nanoparticles, from which the average and standard deviation were calculated accordingly. Standard deviation values are plotted as error bars.

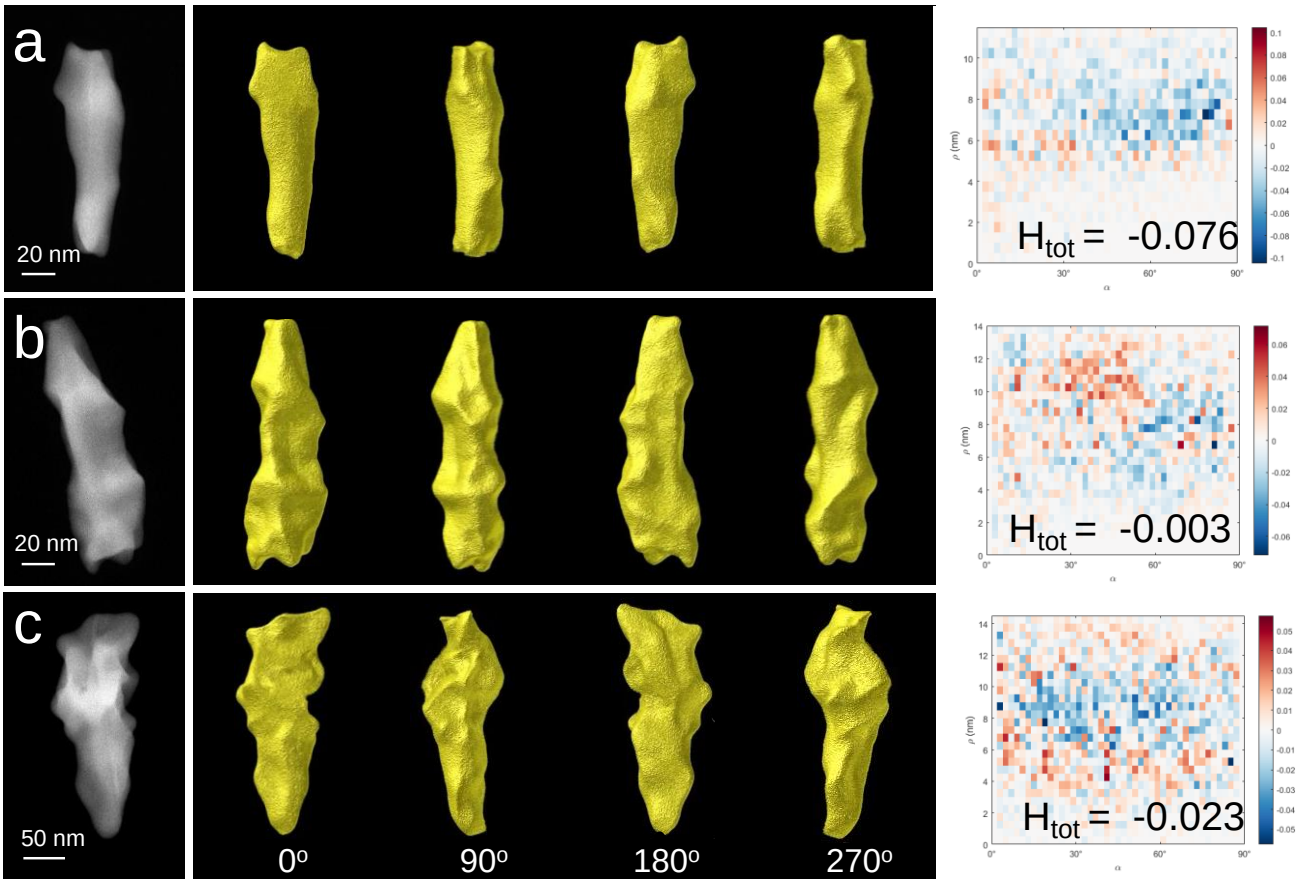

Figure S8. Morphology evolution of PT seeds during multistep growth and the corresponding helicity calculations. (a) Products obtained with reduced $HAuCl_4$ feeding (1/5 compared to the standard condition) after 1 chiral growth step; (Method: 1.9 mL of CTAC (40mM) was put into a tube, which was followed by adding 1 µL of $HAuCl_4$ (5 mM) (not 5 µL as that in the standard synthesis) and 0.2 mL of ascorbic acid (0.1 M) into the solution. Then 30 µL of *L*-2cys (2.5 µM) was added into the PE tube, followed by 10 µL of seed solution. (b) product obtained after 1 standard chiral growth step; (c) product obtained after 9 chiral growth steps.

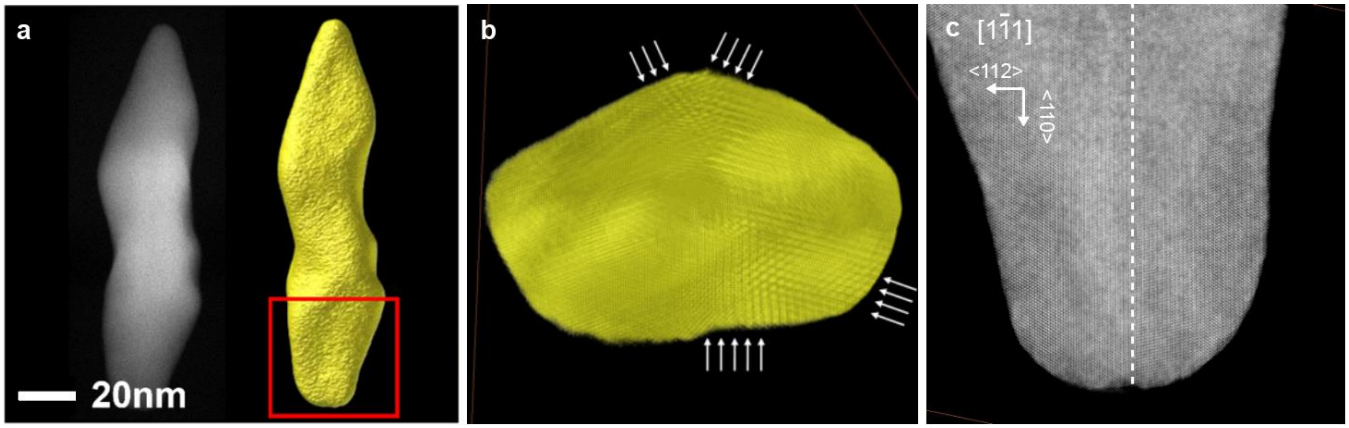

Figure S9. Detail of a PT-Au NR after one growth step. (a) HAADF image of the particle and its electron tomography (ET) results. The red square marks the area for atomic resolution ET measurement. (b) atomic-resolution ET reconstruction of the particle viewed from the bottom. The white arrows indicate the twin-boundaries. (c) Orthoslice through the 3D reconstruction viewed along the [1-11] zone axis. Note that the crystallographic orientations are indicated for one side of the twin boundary (dashed line).

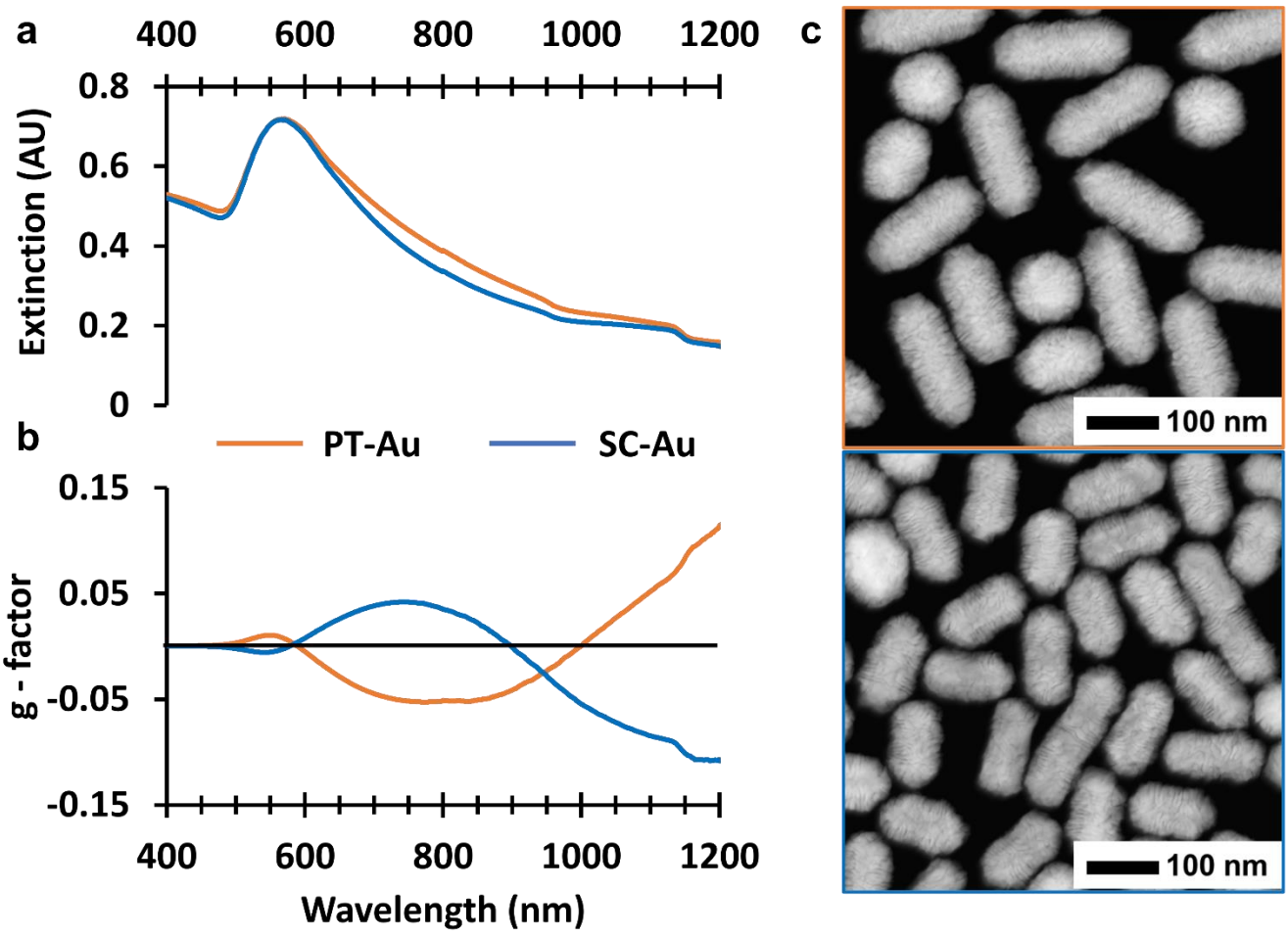

Figure S10. Extinction spectra (a) and chiroptical spectra (b) for chiral particles synthesized using *R*-BINAMINE and PT- or SC-Au NR seeds, as labeled. Right: HAADF STEM characterization of chiral products, image outlines are color-coded to match legend of plot.

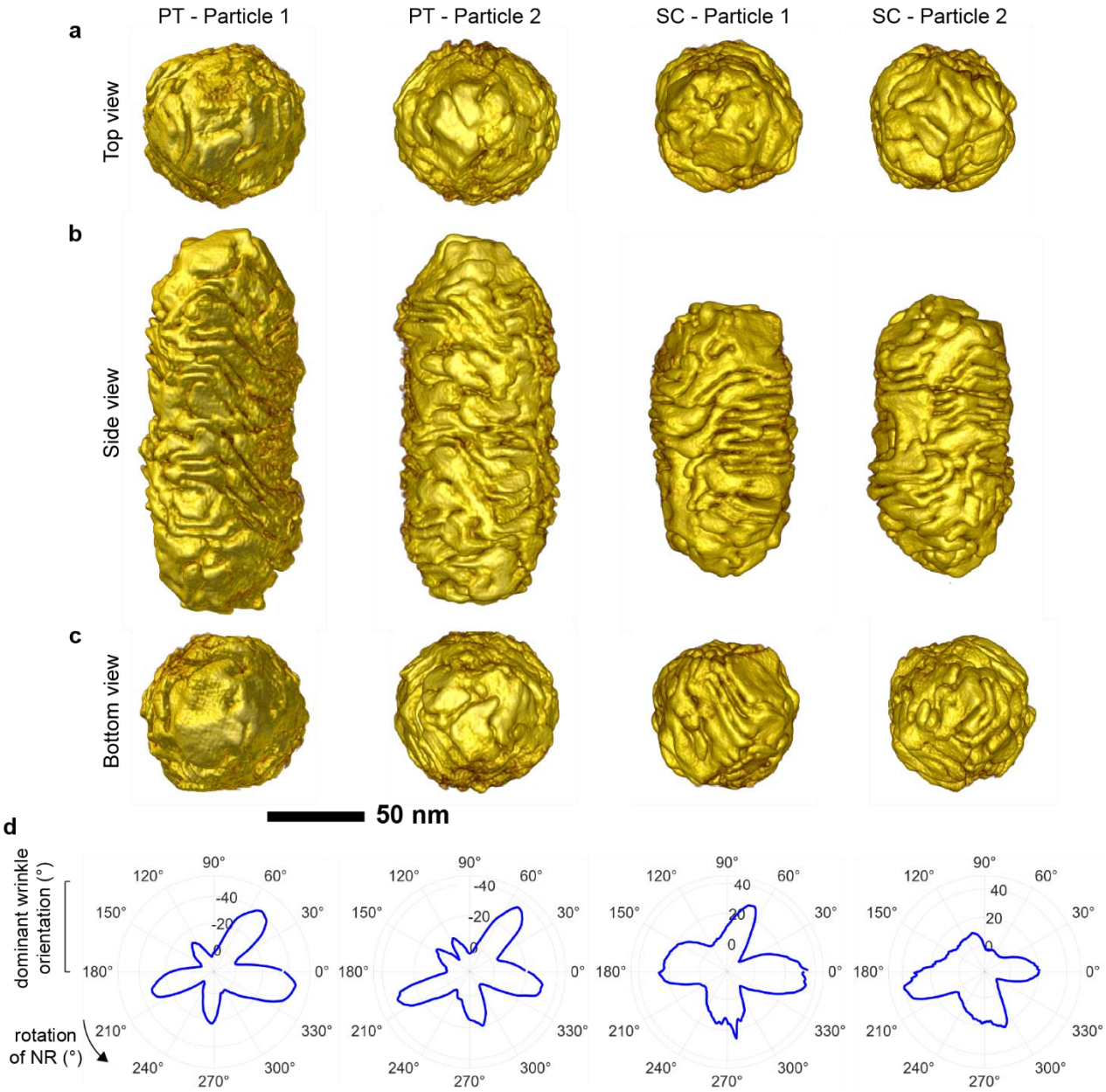

Figure S11. Overview of wrinkled chiral particles obtained from micelle-directed synthesis with *S*-BINANIME and PT or SC seeds as labeled on top. Surface views from (a) the top, (b) the side, (c) the bottom of the particles demonstrating the difference in wrinkle orientation and tip morphology. Note the typically wrinkled tips on SC particles. The scale bar is valid for all views and particles. (d) corresponding plots of the dominant wrinkle orientation as a function of the particle's rotation demonstrating a typically 5-fold rotational symmetry in PT particles and a 4-fold one in SC particles. Note that the radial axis is inverted for PT particles to show increasing magnitude outwards.

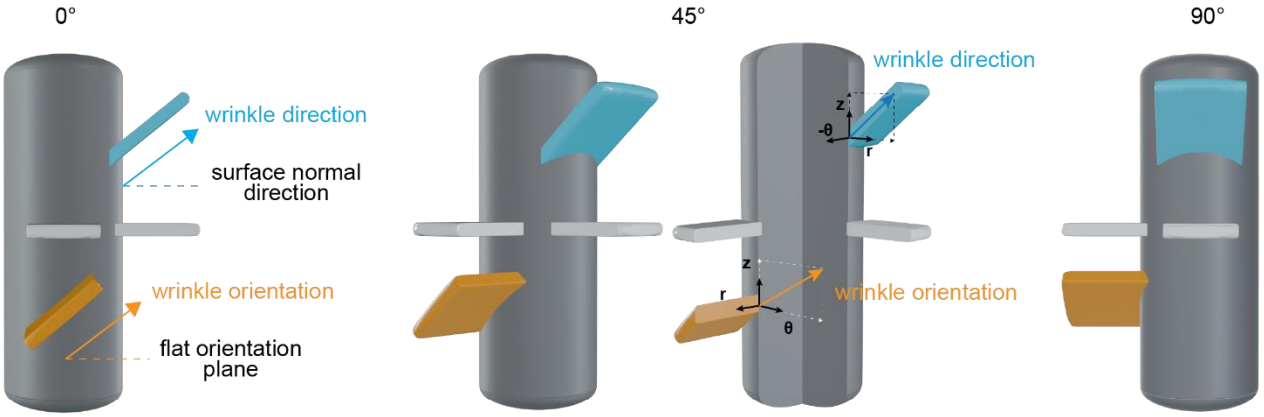

Figure S12. Geometry of wrinkle growth. Two angles are necessary to fully describe Au wrinkles on Au NRs: we define the angle of wrinkle direction with respect to the surface normal when seen in cross section; the wrinkle orientation is the angle with respect to the horizontal plane when NRs are seen from the front with their major axis vertical. Here, the blue wrinkle has a positive direction but 0° orientation, the orange wrinkle has a positive orientation but a 0° direction, the grey wrinkles have neither.

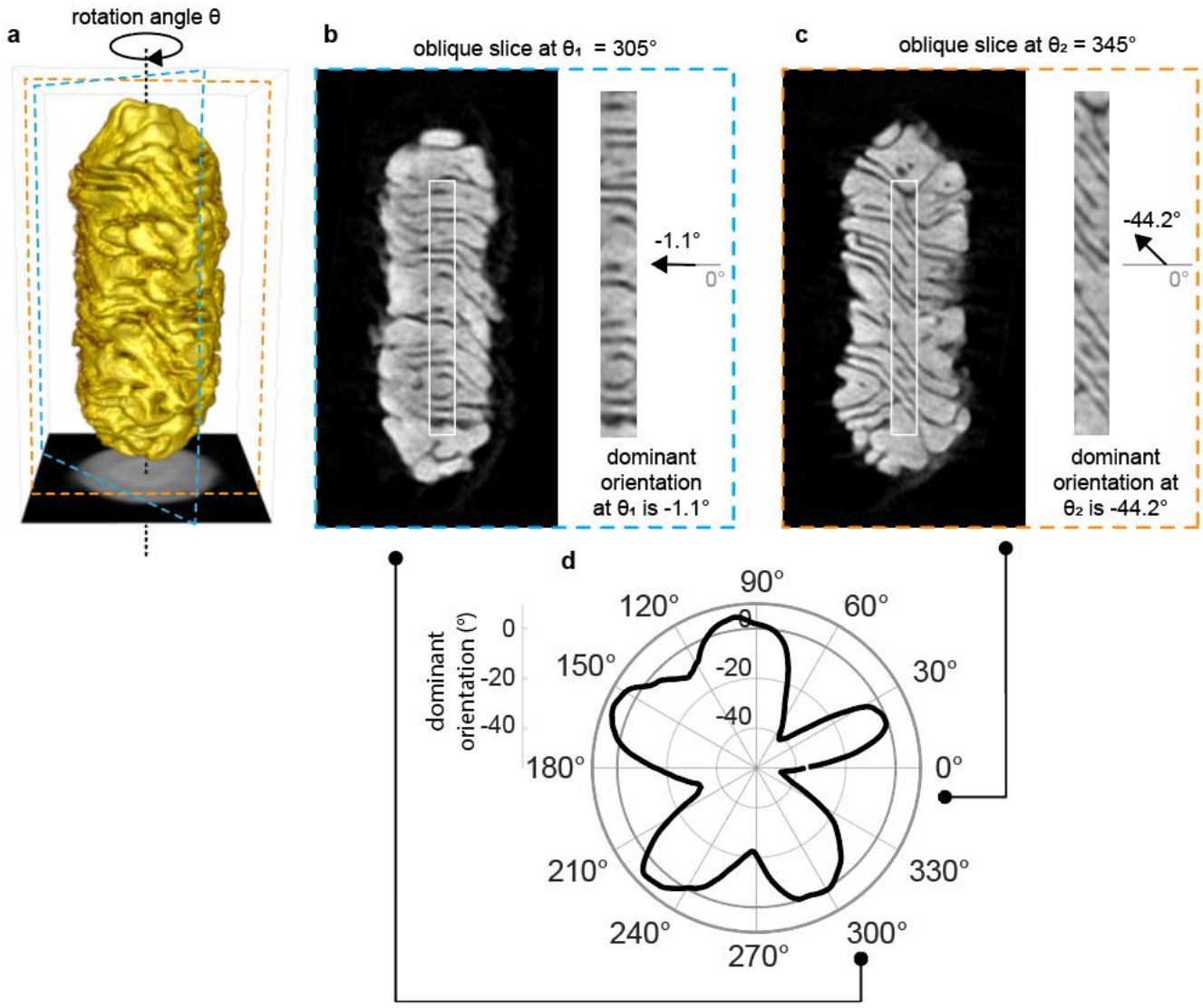

Figure S13. Method for tracking the dominant orientation of the wrinkles. The 3D reconstruction (a) is sliced through the wrinkle corona, 20-30 nm away from the center, for 360 rotation angles θ. The orange and blue dashed lines demonstrate two examples at (b) θ1 = 305° and (c) θ2 = 345°. The dominant orientation is then computed in central areas (white rectangles in (b) and (c)) to prevent bias from the edges of the particle and ensure the metric is specific to a given rotation angle. Assembling the results for all 360 rotational slices yields the polar plots in (d).

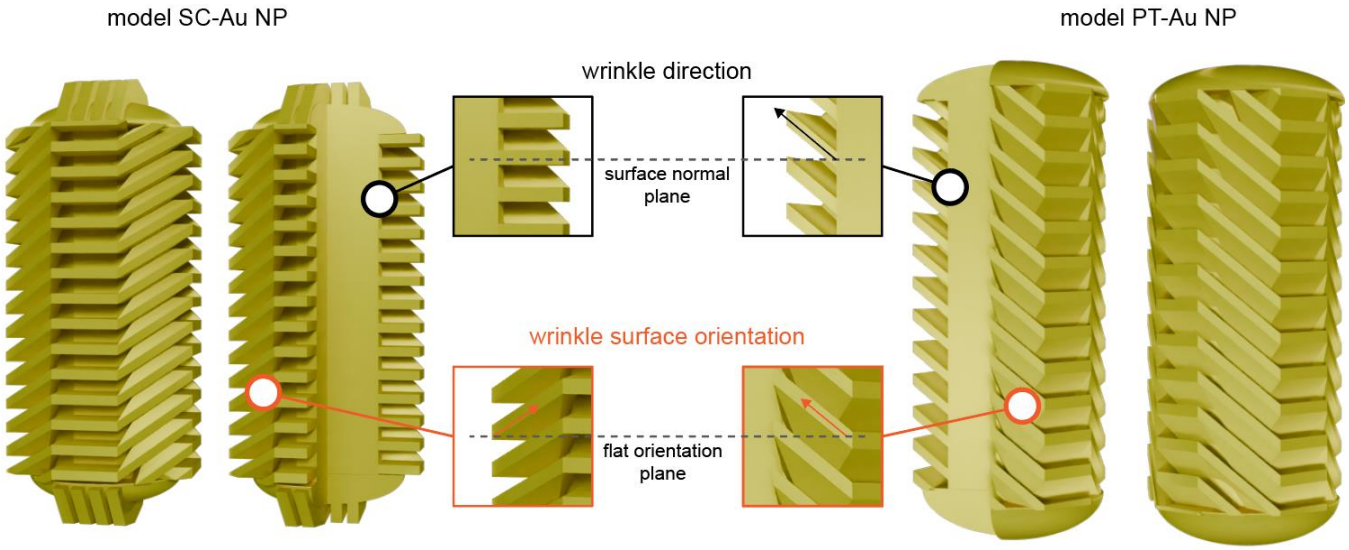

Figure S14. Idealized models of the micelle-templated growth results and example of wrinkle growth direction and wrinkle orientation according to the definitions used herein.